Neural Computing and Applications (2022) 34:11553–11569
https://doi.org/10.1007/s00521-022-07043-5

ORIGINAL ARTICLE

Enhancement and segmentation of medical images through pythagorean fuzzy sets-An innovative approach

R. Premalatha[1] · P. Dhanalakshmi[1]

Received: 7 July 2021 / Accepted: 30 January 2022 / Published online: 2 March 2022

Abstract
Image segmentation has attracted a lot of attention due to its potential biomedical applications. Based on these, in the current research, an attempt has been made to explore object enhancement and segmentation for CT images of lungs infected with COVID-19. By implementing Pythagorean fuzzy entropy, the considered images were enhanced. Further, by constructing Pythagorean fuzzy measures and utilizing the thresholding technique, the required values of thresholds for the segmentation of the proposed scheme are assessed. The object extraction ability of the five segmentation algorithms including current sophisticated, and proposed schemes are evaluated by applying the quality measurement factors. Ultimately, the proposed scheme has the best effect on object separation as well as the quality measurement values.

Keywords Image segmentation · Image enhancement · Thresholding · Pythagorean fuzzy set · Distance measure · Similarity measure · Entropy measure

1 Introduction

COVID-19, the disease caused by SARS-CoV-2, was formally named as a pandemic by the World Health Organization (WHO) [1, 2] in March 2020. COVID-19 is a highly contagious virus that can lead to deadly acute respiratory distress syndrome (ARDS). But there are just a few specific COVID-19 vaccinations available, most unvaccinated persons are susceptible to infection. Early isolation and diagnosis of the infected individual by any legal means is one of the most effective strategies to prevent the spread of viral infection among healthy people. Further, an X-ray or CT scan of the patient's chest is one of the most effective ways to detect this virus. In addition, lung inflammation can be dangerous to people's health. The rising number of infected persons in the community needs more effective therapies as well as a cost-effective process based on the primary diagnosis. The ability to recognize contaminated tissue quickly and precisely is critical for optimal patient treatment and survival [3–6].

CT provides a pathophysiology guide, which may aid in the diagnosis and progression of various disease stages. It develops to become a viable diagnostic tool for treating COVID-19-related lung infection in medical practice [7]. According to early studies, chest CT provides high sensitivity for detecting COVID-19 lung disease. As per the article, [8], several organizations have proven the ability to diagnose using CAD systems with an accuracy of up to 95%. Nowadays, medical imaging has just been exploited for a variety of disease diagnostics. Medical imaging technologies may also be employed as a key pathological tool that helps for identifying possible diseases.

On the other hand, digital images are commonly illustrated by utilizing computer-based image processing. The intensity of each image element in a digital image is reported by a numerical integer. In general, the purpose of image processing is to transform the source image into a more informative image with the aid of mathematically manipulated recorded numerical integers. In practice, this is performed by subjecting the source image to appropriate mathematical functions and saving the effects of the calculation as a new image. The mathematical mechanisms employed in image processing are almost limitless, but a wide variety of mechanisms can be classified into one of four major functions: thematic classification, image

✉ R. Premalatha
premalatha.appliedmaths@buc.edu.in

[1] Department of Applied Mathematics, Bharathiar University, Coimbatore 641046, India

restoration, image segmentation, and image enhancement. At this, image enhancement mechanisms [9] try to improve the detection of patterns or objects in an image. The authors [10] suggested the image enhancement mechanism and analysis for the satellite images. Ram et al. [11] proposed polarization-based spatial filtering for the edge enhancement approach utilizing S-waveplate. Further, enhancement and classification based on brain MRI images have been done in [12]. Zhong et al. [13] recommended an image enhancement technique based on wavelet analysis and new pseudo-color image processing for the black-and-white image. The author [14] offered a contrast enhancement mechanism is enforced to improve image contrast, descriptive ability, and image appearance by increasing the gray level range. And also, the enhanced images are usually comfortable to interpret than the source images.

Image segmentation refers to the division of a digital image into several parts, which is a simple and significant tool in digital image processing. The main purpose of segmentation is to transform the images into more meaningful parts, separating objects from the background and locating image edges. The great applications in this field are as image denoising, face detection, video surveillance, fingerprint recognition, iris recognition, machine vision, content-based image retrieval, and brake light detection, locate objects (roads, forests, and crops) in satellite images [15], and particularly in the domain of medical imaging [16]. Recently, there have been several division methods and procedures in the literature, some of which include: edge detection, clustering, thresholding, region-growing methods, dual clustering method, histogram-based methods, watershed transformation, and so on. Each of the aforementioned methods is based on some methodologies for partitioning regions of the image.

Thresholding is a fascinating object separation mechanism that is also the most widely used, well-known, and dependable technique for image segmentation analysis. This mechanism works on a noisy image, converting the grey image to a binary image with a threshold value and this threshold value serves as the key feature of this mechanism. Over the past few decades, the choice of threshold has been based on certain statistical characteristics [17, 18], such as minimum error approach, entropy approach, moment-based algorithm, and class variation systems. The above statistical term class variance system limits the high computational time and cost. Following that, some thresholding approaches fail in a unimodal distribution as well as incapable of determining the threshold for imprecise data in an image; these issues are addressed by recommending the use of non-linear thresholds based on a fuzzy rule (multi-dimensional). Vague/imprecise image object is separated using the fuzzy set (FS) theory provided by Zadeh [19]. The authors [20] suggested a scheme to extract the image based on the FS approach instead of the crisp set. As a result, the entire image in the form of the FS, as well as each of their image elements (grey pixel), has a membership value. Under those circumstances, the membership function plays a vital role in the separation of the image object, and it is defined in terms of the unique characteristics of the image. As evidenced in [21, 22], there is rich literature on FS-based image thresholding techniques. Later, Atanassov [23] suggested that the new FS be an Intuitionistic Fuzzy Set (IFS), with two degrees of membership and non-membership for each component. Moreover, the author Yager [24, 25] proposed the Pythagorean Fuzzy Set (PFS), an extension of IFS in which each element is represented by a pair of membership and non-membership degrees. Image segmentation employs a variety of membership and non-membership functions [21, 26–28], including the Gamma, triangular, Sugeno, and Yager.

Notably, in reference, the primary goal is to achieve image segmentation by optimizing the threshold with the fuzzy measure and calculating the appropriate membership function of the original image prior to applying the fuzzy measure. Different fuzzy threshold selection measures, such as the entropy measure [22], the similarity score function [29], and the divergence measure [30] have recently flourished, and these solve the problem of separation in imprecise images. The thresholding based on similarity measure is an appealing mechanism that is employed as an elementary tool to determine the threshold in an image [29, 31]. In the literature, the PFS-based similarity, distance, and entropy measures are discussed [32–35]. The main aspiration for using similarity-based thresholding is that a particular object is associated with the same grey levels in the image's pixels. Thresholding mechanisms like these are used to classify the foreground (Fg) and background (Bg) into different groups.

Inspired by the previous conceptions, image enhancement from the PFS feature and the segmentation of two-dimensional biomedical images such as lungs affected due to the COVID-19 virus has been effectively demonstrated in this article. The proposed scheme is divided into two steps: image enhancement and division. After activating the Pythagorean fuzzy (PFS) entropy, the aforesaid clinical images were properly enhanced. Further, enhanced images are employed for the purpose of the extraction process, which determines the thresholds that separate the object from the background. Furthermore, the proposed and other object extraction schemes, such as Method1 [4], Method2 [5], Method3 [6], Method4 [7] are compared with each other with the aid of quality measurement factors. According to the results of the aforementioned analysis, the proposed PFS-based object extraction technique performs admirably in terms of segmentation and factor values.

The following is the overall framework for this study. Section 2 investigates the theoretical background like PFS-based image enhancement and segmentation. In Sect. 3, objective analysis is discussed. Section. 4 expresses the experimental results and analysis. Finally, in Sect. 5, the concluding annotations are written.

2 Theoretical background

2.1 Pythagorean fuzzy set

A fascinating novel system revealed by Yager [24], the Pythagorean fuzzy theory is a formidable scheme and it has freshly become attractive. Pythagorean Fuzzy Theory (PFT) is proposed by an aspect of the Fuzzy set theory (FST). In PFT, situations are categorized and explored under three factors: 'Membership', 'Non-membership', and 'indeterminacy'. In PFS's view, it is a beneficial device to solve the indeterminacy issues, which has been employed in the applications of image processing namely, edge detection, segmentation, and so on.

2.2 Pythagorean fuzzy image (PFI)

The source RGB image has been altered to a grayscale image and the altered image is again reconfigured in the design of PFS, which holds the factors such as membership 'μ', indeterminacy 'π', and non-membership 'v'. In that, there are foreground (Fg) in μ, background (Bg) in v, and ambiguities or edges (Ed) belongs to π in the grayscale domain. Later, the Fg, Bg, and Ed regions must be obtained by executing the functions μ, v, and π. The foreground division is being carried out in the final stages.

2.3 Image enhancement

Firstly, in order to build a PFS from IFS, PFI is formed. The efficient strategy of PFI is the formulation of membership and non-membership functions of the image. In the beginning process, the grayscale image $\mathbb{A}$ is fuzzified by the upcoming formula:

$$\mu_{\mathbb{A}}(gl) = \frac{gl(r,c) - gl_{min}}{gl_{max} - gl_{min}} \tag{1}$$

Here, $gl(r, c)$ is the gray picture element at the location (r, c). The notations gl_{min} and gl_{max} are the minimum and maximum intensities of the image $\mathbb{A}$.

2.3.1 μ, v, and π degrees estimation

Based on the IFS, the degree of membership is estimated by applying the following generator [14]:

$$\mu_{\mathbb{A}}^{PFS}(gl(r,c);\lambda) = 1 - \frac{1-\mu_{\mathbb{A}}(gl)}{1+(e^{\lambda}-1)\mu_{\mathbb{A}}(gl)}, \lambda > 0. \tag{2}$$

Then implementing the fuzzy negation $\Psi(x) = \frac{1-x}{1+(e^{\lambda}-1)x}$, $\lambda > 0$, the degree of non-membership in the PFI is estimated as:

$$\begin{aligned} v_{\mathbb{A}}^{PFS}(gl(r,c);\lambda) &= \Psi(\mu_{\mathbb{A}}^{PFS}(gl(r,c);\lambda)) \\ v_{\mathbb{A}}^{PFS}(gl(r,c);\lambda) &= \frac{1-\mu_{\mathbb{A}}^{PFS}(gl(r,c);\lambda)}{1+(e^{\lambda+1}-1)\mu_{\mathbb{A}}^{PFS}(gl(r,c);\lambda)}, \lambda > 0 \end{aligned} \tag{3}$$

Finally, the degree of indeterminacy in the PFI is estimated as

$$\begin{aligned} &\pi_{\mathbb{A}}^{PFS}(gl(r,c);\lambda) \\ &= \sqrt{1-(\mu_{\mathbb{A}}^{PFS}(gl(r,c);\lambda))^2 - (v_{\mathbb{A}}^{PFS}(gl(r,c);\lambda))^2} \end{aligned} \tag{4}$$

2.3.2 Entropy

Entropy act as a significant part of image processing. The authors De Luca and Termini [36] first recommended non-probabilistic entropy in the FS environment. Moreover, the authors [35] offered numerous entropy measurements by employing PFT. In this study, the Pythagorean Fuzzy Entropy (PFE) is implemented and its mathematical formula is as follows:

$$\begin{aligned} PFE(\mathbb{A};\lambda) = &\frac{1}{|\mathbb{R}\times\mathbb{C}|} \\ &\sum_{r=0}^{\mathbb{R}}\sum_{c=0}^{\mathbb{C}} \frac{(\pi_{\mathbb{A}}^{PFS}(gl(r,c);\lambda))^2 + 1 - |(\mu_{\mathbb{A}}^{PFS}(gl(r,c);\lambda))^2}{(\pi_{\mathbb{A}}^{PFS}(gl(r,c);\lambda))^2 + 1 + |(\mu_{\mathbb{A}}^{PFS}(gl(r,c);\lambda))^2} \\ &\frac{-(v_{\mathbb{A}}^{PFS}(gl(r,c);\lambda))^2|}{-(v_{\mathbb{A}}^{PFS}(gl(r,c);\lambda))^2|} \end{aligned} \tag{5}$$

PFE is measured by utilizing the above equation (5) for each λ value. Likewise, the maximum value of PFE corresponds to the λ value, is considered as optimum value, which is written by:

$$\lambda_{opt} = \max\ (PFE(\mathbb{A};\lambda)) \tag{6}$$

Here, the measured value λ_{opt} is substituted in equation (2), then the equation is of the mathematical form as follows:

$$\mu_{\mathbb{A}}^{PFS}(gl) = 1 - \frac{1-\mu_{\mathbb{A}}(gl)}{1+(e^{\lambda_{opt}}-1)\mu_{\mathbb{A}}(gl)} \tag{7}$$

Further, the Pythagorean fuzzy image is constructed.

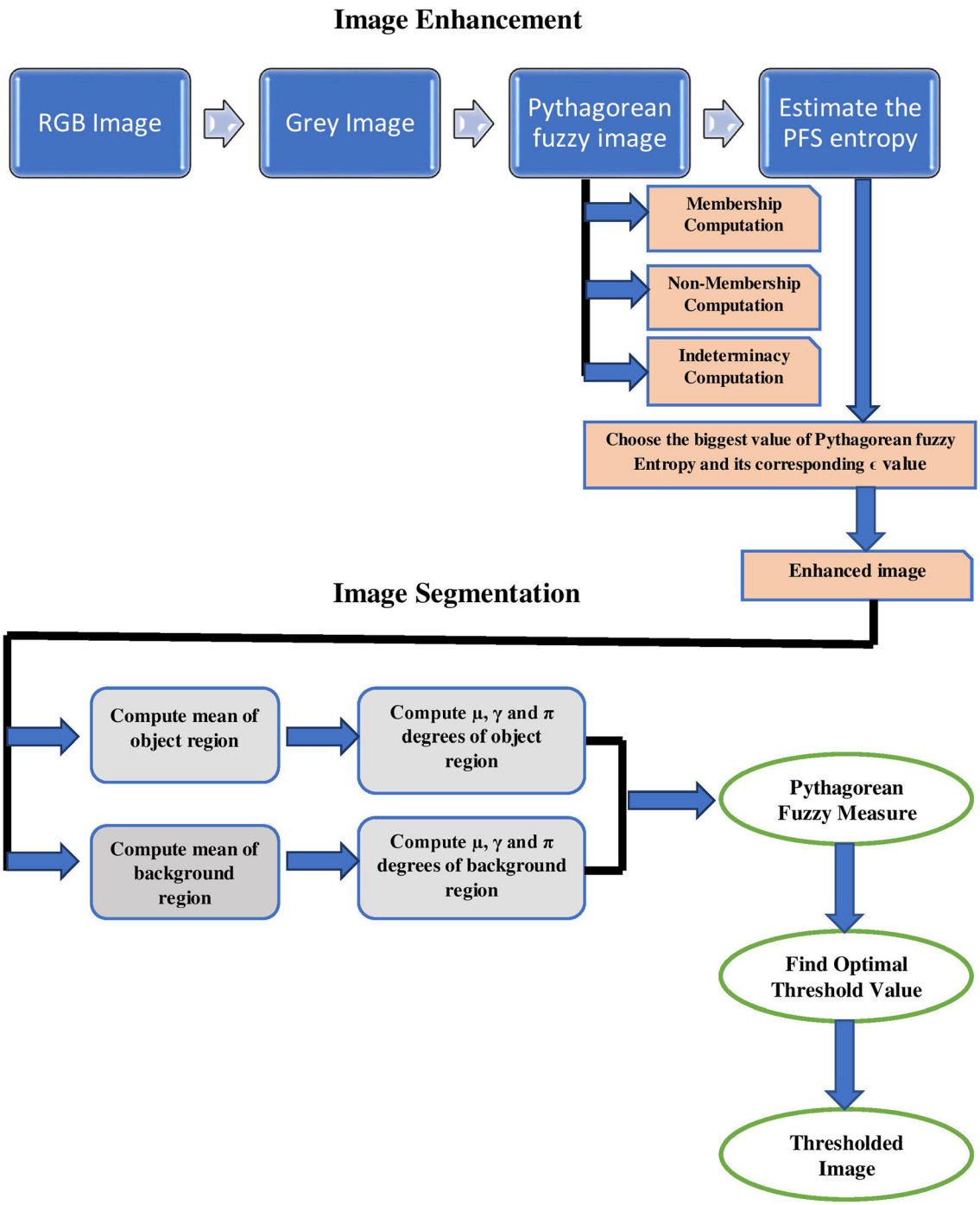

Fig. 1 Schematic representation of the proposed image segmentation process

2.3.3 Enhancement

The PFI is utilized in the image enhancement process and their mathematical term is written as:

$$\mathbb{A}^{\text{enh}}(\text{gl}(\text{r},\text{c})) = \begin{cases} 2[\mu_{\mathbb{A}}^{\text{PFS}}(\text{gl}(\text{r},\text{c}))]^2; & \text{if } \mu_{\mathbb{A}}^{\text{PFS}}(\text{gl}(\text{r},\text{c})) \le 0.5 \\ 1-2[1-\mu_{\mathbb{A}}^{\text{PFS}}(\text{gl}(\text{r},\text{c}))]^2; & \text{if } 0.5 < \mu_{\mathbb{A}}^{\text{PFS}}(\text{gl}(\text{r},\text{c})) \le 1 \end{cases} \tag{8}$$

The aforementioned equation (8) forms the contrast enhanced image.

2.4 Image segmentation

In general, every image contains unimodal, bimodal, trimodal, and multimodal regions according to the intensity range. Bimodal images need a single threshold for image

segmentation and trimodal, multimodal images need two or more thresholds to segment the images. In this, multimodal images are taken into account. The segmentation algorithm is shown in Fig. 1. In the aforementioned figure, the best threshold values are obtained using the PFS measure between the manually thresholded image and the enhanced thresholded image. The manually thresholded image is that image in which each pixel strictly belongs to its respective (object or background) regions. In that, each pixel has a degree of membership as 1 and its degrees of non-membership and hesitation are 0. The threshold selection algorithm is illustrated by the following steps.

Step 1 The search process is to find the optimal threshold value, and this mechanism requires only single for loop with T varying from 0–255.

Step 2 The enhanced image $\mathbb{A}^{enh}$ of dimension $\mathbb{R} \times \mathbb{C}$ and let the symbol '$\mathscr{L}$' indicates the levels of the grayness of the image $\mathbb{A}^{enh}$ that is $\mathscr{L} = \{0, 1, ..., \mathbb{L}-1\}$, where $\mathbb{L}$ specifies the maximum gray level of $\mathbb{A}^{enh}$. $\mathbb{N}(gl)$ denotes the frequency of the gray level 'gl'.

Step 3 The pixels of the enhanced image $\mathbb{A}^{enh}$ are splited in two classes, namely foreground (Fg) and background (Bg). The notation 'Bg' exposes the set of pixels accompanied with the intensity values $\{0, 1, ..., t\}$ and 'Fg' expresses the set of pixels accompanied with the intensity values $\{t+1, ..., \mathbb{L}-1\}$ where 't 'specifies the threshold value.

Step 4: The mean of the Fg and Bg classes are expressed as follows:

$$m_1 = \frac{\sum_{gl=0}^{t} gl\mathbb{N}(gl)}{\sum_{gl=0}^{t} \mathbb{N}(gl)} \text{ and } m_2 = \frac{\sum_{gl=t+1}^{\mathbb{L}-1} gl\mathbb{N}(gl)}{\sum_{gl=t+1}^{\mathbb{L}-1} \mathbb{N}(gl)} \tag{9}$$

Here m_1 and m_2, respectively, denote the average values of Bg and Fg classes.

Step 5: This paper considers the gamma distribution for experimental purposes because it ensures the images to symmetric nature. Then, each image element (r, c) membership value in the enhanced image $\mathbb{A}^{enh}$ is determined by applying Gamma distribution [21] as follows:

$$\mu_{\mathbb{A}}^{enh}(gl(r,c)) = \begin{cases} \exp\ (-c_1^*.|gl(r,c) - m_1|) & \text{if } gl(r,c) \le t \\ \exp\ (-c_1^*.|gl(r,c) - m_2|) & \text{if } gl(r,c) > t2 \end{cases} \tag{10}$$

Here, m_1 and m_2 are the mean intensity for two regions of the $(r,c)^{th}$ pixel, and the constant $c_1^* = \frac{1}{(\max\ (gl) - \min\ (gl))}$. For multilevel thresholding, since there are n-regions in the image, $n-1$ threshold values ($t1$, $t2$,..., $tn-1$) were chosen such that $0 \le t1 < t2 < ... < tn-1 \le \mathbb{L}-1$, whereby $\mathbb{L}$ is just the image's maximum grey level. Following the notion of bilevel thresholding, in the case of multilevel thresholding, the membership function will take the form:

$$\mu_{\mathbb{A}}^{enh}(gl(r,c)) = \begin{cases} \exp\ (-c_2^*.|gl(r,c) - m_1|) & \text{if } gl(r,c) \le t \\ \exp\ (-c_2^*.|gl(r,c) - m_2|) & \text{if } t1 < gl(r,c) \le t2 \\ \vdots & \vdots \\ \exp\ (-c_2^*.|gl(r,c) - m_n|) & \text{if } gl(r,c) > tn-1 \end{cases} \tag{11}$$

Here, the average grey levels for the n-regions partitioned by that of the thresholds $t1$, $t2$, ..., $tn-1$ are m_1, m_2, ..., m_n, as well as the constant c_2^*, is much like c_1^* in Equation (10).

Step 6 Each image element (r, c) non-membership value in the enhanced image $\mathbb{A}^{enh}$ is computed by employing Sugeno's generator (Sugeno [26]) as follows:

$$v_{\mathbb{A}}^{enh}(gl(r,c)) = \frac{1 - \mu_{\mathbb{A}}^{enh}(gl(r,c))}{1 + \zeta.\mu_{\mathbb{A}}^{enh}(gl(r,c))}; \zeta > 0. \tag{12}$$

Step 7: Each image element (r, c) indeterminacy value in the enhanced image $\mathbb{A}^{enh}$ is illustrated by implementing the above equations (10) and (12), which can be written in the following form:

$$\pi_{\mathbb{A}}^{enh}(gl(r,c)) = \sqrt{1 - [(\mu_{\mathbb{A}}^{enh}(gl(r,c)))^2 + (v_{\mathbb{A}}^{enh}(gl(r,c)))^2]} \tag{13}$$

where $\pi_{\mathbb{A}}^{enh}(gl(r,c))$ indicates the degree of indeterminacy of the image $\mathbb{A}^{enh}$.

Step 8:This paper utilizes the measure [32] provided below to determine the degree of similarity between the manually thresholded image and the enhanced thresholded image with the threshold t.

$$\mathbb{S}(\mathbb{A},\mathbb{B}) = 1 - \left\{ \frac{1}{\mathbb{R}\times\mathbb{C}} \sum_{r=0}^{\mathbb{R}-1} \sum_{c=0}^{\mathbb{C}-1} \left\{ \begin{array}{l} \frac{1}{4}\left\{ \begin{array}{l} \left|(\mu_{\mathbb{A}}^{enh}(gl(r,c)))^2 - (\mu_{\mathbb{B}}^{enh}(gl(r,c)))^2\right|^{\tau} + \\ \left|(v_{\mathbb{A}}^{enh}(gl(r,c)))^2 - (v_{\mathbb{B}}^{enh}(gl(r,c)))^2\right|^{\tau} + \\ \left|\pi_{\mathbb{A}}^{enh}(gl(r,c)))^2 - (\pi_{\mathbb{B}}^{enh}(gl(r,c)))^2\right|^{\tau} \end{array} \right\}_{+} \\ \frac{1}{2}\max\left\{ \begin{array}{l} \left|(\mu_{\mathbb{A}}^{enh}(gl(r,c)))^2 - (\mu_{\mathbb{B}}^{enh}(gl(r,c)))^2\right|^{\tau} \\ \left|(v_{\mathbb{A}}^{enh}(gl(r,c)))^2 - (v_{\mathbb{B}}^{enh}(gl(r,c)))^2\right|^{\tau} \\ \left|(\pi_{\mathbb{A}}^{enh}(gl(r,c)))^2 - (\pi_{\mathbb{B}}^{enh}(gl(r,c)))^2\right|^{\tau} \end{array} \right\} \end{array} \right\}^{\frac{1}{\tau}}, \tau \ge 1 \tag{14}$$

Now, if $\mathbb{A}^{enh}$ is the enhanced thresholded image and $\mathbb{B}^{enh}$ is the manually thresholded image, then $\mu_{\mathbb{B}}^{enh}(gl(r,c)) = 1$, $v_{\mathbb{B}}^{enh}(gl(r,c)) = 0$ and $\pi_{\mathbb{B}}^{enh}(gl(r,c)) = 0$. Hence, equation. (14) is reduced, which is denoted in the form as

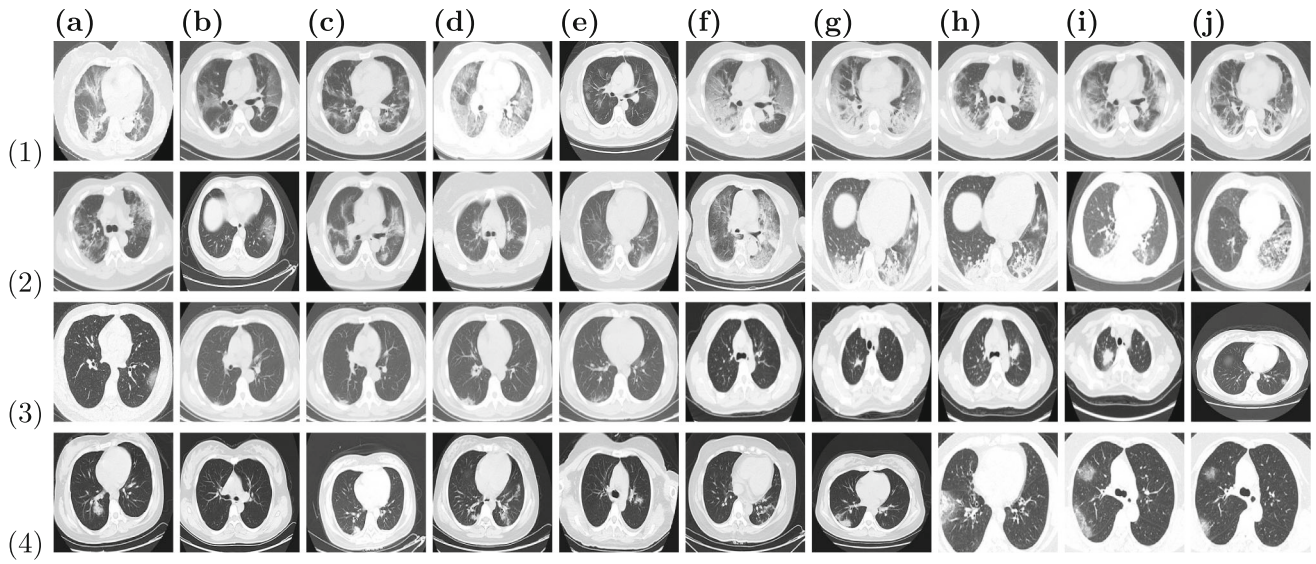

Fig. 2 Source images: CT scan of lungs affected by COVID-19 [Above 50% ((1a)-(2j)) and Below 50% ((3a)–(4j))]

$$\mathbb{S}(\mathbb{A},\mathbb{B}) = 1 - \left\{ \frac{1}{\mathbb{R}\times\mathbb{C}} \sum_{r=0}^{\mathbb{R}-1} \sum_{c=0}^{\mathbb{C}-1} \left\{ \begin{array}{l} \frac{1}{4}\left\{ \begin{array}{c} \left|(\mu_{\mathbb{A}}^{enh}(gl(r,c)))^2 - 1\right|^{\tau} + \\ \left|(v_{\mathbb{A}}^{enh}(gl(r,c)))^2\right|^{\tau} + \\ \left|\pi_{\mathbb{A}}^{enh}(gl(r,c)))^2\right|^{\tau} \end{array} \right\} + \\ \frac{1}{2}\max\left\{ \begin{array}{c} \left|(\mu_{\mathbb{A}}^{enh}(gl(r,c)))^2 - 1\right|^{\tau}, \\ \left|(v_{\mathbb{A}}^{enh}(gl(r,c)))^2\right|^{\tau}, \\ \left|(\pi_{\mathbb{A}}^{enh}(gl(r,c)))^2\right|^{\tau} \end{array} \right\} \end{array} \right\}^{\frac{1}{\tau}} \right\}, \tau \geq 1 \tag{15}$$

Step 9: Calculate the max($\mathbb{S}(\mathbb{A},\mathbb{B})$), the resultant value corresponding to the gray value is considered as an optimal threshold $\mathfrak{t}$.

Step 10: Employ the obtained optimal threshold t in the enhanced image $\mathbb{A}^{enh}$ to produce the thresholded (segmented) image $\mathbb{A}^{seg}$.

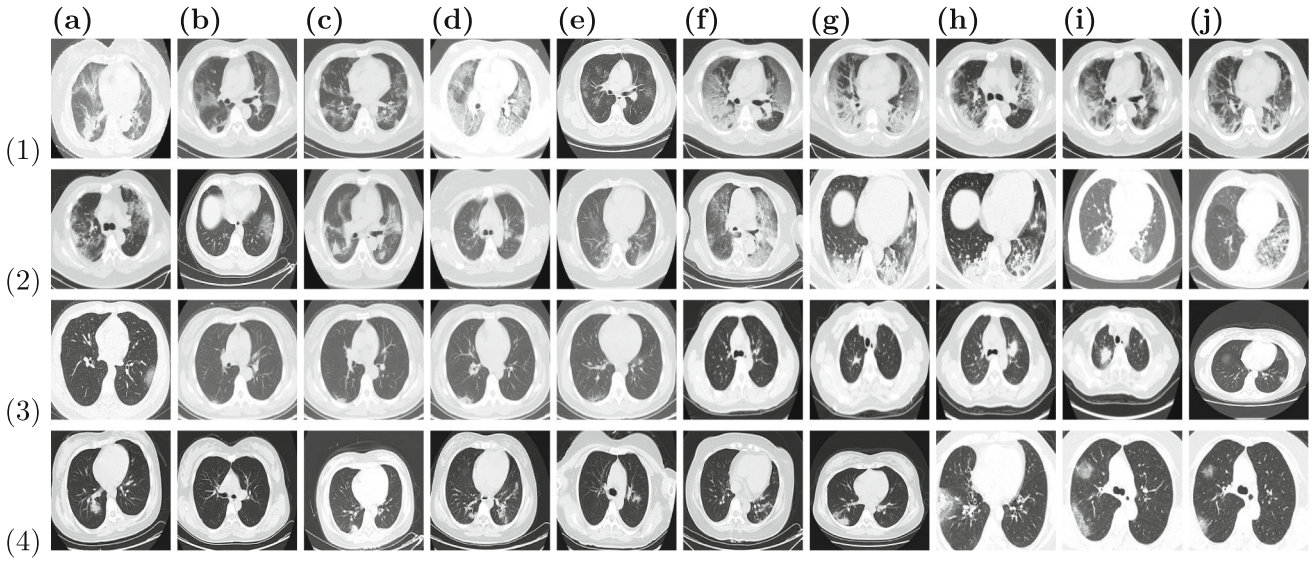

Fig. 3 Gray images: CT scan of lungs affected by COVID-19 [Above 50% ((1a)-(2j)) and Below 50% ((3a)–(4j))]

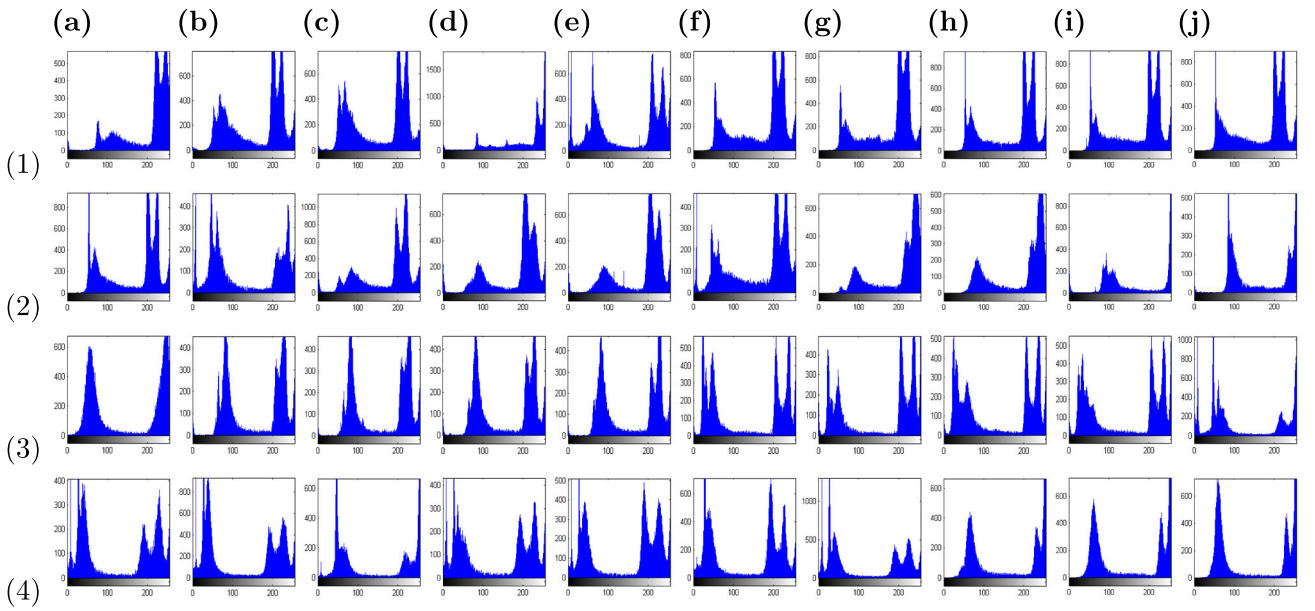

Fig. 4 Histogram: CT scan of lungs affected by COVID-19 [Above 50% ((1a)-(2j)) and Below 50% ((3a)–(4j))]

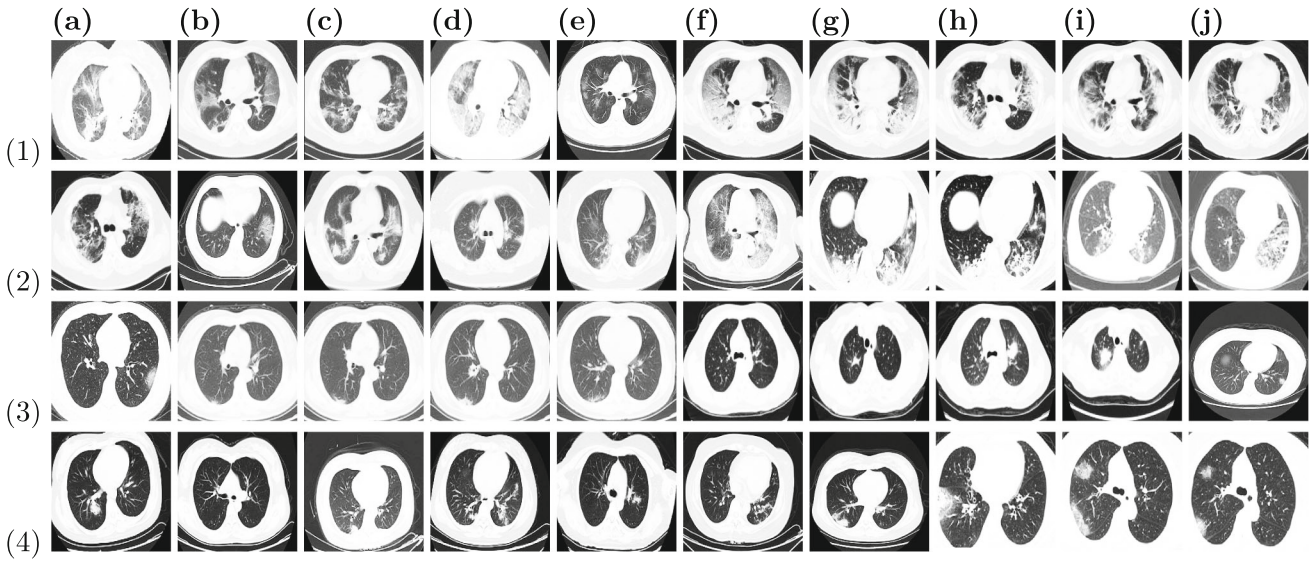

Fig. 5 Enhanced images: CT scan of lungs affected by COVID-19 [Above 50% ((1a)-(2j)) and Below 50% ((3a)–(4j))]

3 Objective analysis

Image quality evaluation measures are applied to obtain the efficacy of the proposed scheme in comparison with other existing works.

3.1 Mean absolute error (MAE)

Deviations from thresholded and manually thresholded images are measured in MAE, and the mathematical form is given below

$$MAE = \frac{1}{\mathbb{R} \times \mathbb{C}} \sum_{r=1}^{\mathbb{R}} \sum_{c=1}^{\mathbb{C}} \left| \mathbb{A}^{seg}(gl(r,c)) - \mathbb{B}^{seg}(gl(r,c)) \right| \tag{16}$$

Here, $\mathbb{B}^{seg}(gl(r,c))$, and $\mathbb{A}^{seg}(gl(r,c))$ mentions the manually thresholded image and thresholded image utilizing proposed scheme in the pixel $gl(r, c)$. If the above equation (16) delivers the minimum deviation (zero or near to zero), then both images $\mathbb{A}^{seg}(gl(r,c))$, and $\mathbb{B}^{seg}(gl(r,c))$ are more similar. Or else the images are not identical.

Table 1 Threshold Values

Lungs affected by above 50% due to COVID-19						Lungs affected by below 50% due to COVID-19					
S.no	Method1	Method2	Method3	Method4	Proposed	**S.no**	Method1	Method2	Method3	Method4	Proposed
1	41, 122, 207	40, 120, 202	43, 123, 208	39, 118, 205	41, 125, 210	21	152	154	156	149	157
2	57, 98, 151, 213	57, 95, 148, 210	57, 103, 156, 219	53, 94, 147, 209	60, 101, 154, 217	22	71, 123, 202	71, 120, 199	71, 128, 207	68, 119, 198	74, 126, 205
3	71, 130, 206	70, 127, 203	74, 133, 209	67, 126, 202	71, 135, 211	23	69, 121, 201	68, 118, 198	72, 124, 204	65, 117, 197	69, 126, 206
4	42, 109, 173, 229	42, 106, 170, 226	42, 114, 178, 234	38, 105, 169, 225	45, 112, 176, 232	24	70, 121, 201	69, 118, 198	70, 126, 206	66, 117, 197	73, 124, 204
5	36, 103, 196	35, 100, 193	39, 106, 199	32, 99, 192	36, 108, 201	25	111, 196	110, 193	114, 199	107, 192	111, 201
6	105, 198	104, 195	105, 203	101, 194	109, 201	26	25, 66, 136, 215	24, 63, 133, 212	25, 71, 141, 222	21, 62, 132, 211	28, 69, 139, 218
7	82, 149, 214	81, 146, 211	85, 152, 217	78, 145, 210	82, 153, 219	27	28, 95, 198	27, 92, 195	31, 99, 201	24, 91, 194	28, 100, 203
8	82, 148, 214	81, 145, 211	82, 153, 219	78, 144, 210	85, 151, 217	38	39, 109, 202	38, 106, 198	39, 114, 207	35, 105, 197	42, 112, 205
9	83, 149, 214	82, 146, 211	83, 154, 219	79, 145, 210	83, 153, 218	29	38, 111, 204	37, 108, 201	41, 114, 207	34, 107, 200	38, 116, 209
10	101, 194	100, 194	99, 199	98, 190	102, 197	30	23, 64, 120, 204	22, 61, 117, 201	23, 69, 125, 209	19, 60, 116, 200	26, 67, 123, 207
11	11, 140, 210	77, 137, 207	80, 143, 213	74, 136, 206	77, 145, 215	31	27, 88, 183, 242	26, 85, 180, 240	30, 91, 184, 245	23, 84, 179, 239	27, 93, 188, 247
12	25, 67, 126, 207	25, 64, 123, 204	25, 72, 131, 212	21, 64, 122, 203	28, 70, 129, 210	32	24, 65, 133, 212	23, 62, 130, 210	24, 69, 138, 215	20, 61, 129, 209	27, 68, 137, 215
13	42, 102, 160, 217	41, 99, 160, 214	45, 105, 163, 220	38, 98, 156, 213	42, 107, 165, 222	33	60, 122, 208	69, 118, 205	63, 125, 211	56, 117, 204	60, 127, 213
14	44, 121, 201	43, 118, 198	44, 126, 206	40, 117, 197	47, 124,204	34	28, 72, 138, 213	27, 69, 135, 210	28, 77, 143, 218	24, 68, 134, 209	31, 75, 141, 216
15	43, 117, 198	42, 114, 195	47, 120, 201	39, 114, 194	43, 122, 203	35	26, 86, 180, 243	25, 83, 177, 240	29, 89, 183, 246	22, 82, 176, 239	26, 91, 185, 248
16	63, 131, 206	62, 128, 202	63, 136, 211	59, 127, 202	66, 134, 209	36	27, 66, 133, 209	26, 63, 130, 206	27, 71, 139, 214	23, 62, 129, 205	30, 69, 136, 212
17	121, 209	120, 204	124, 211	117, 213	121, 212	37	30, 83, 177, 224	29, 82, 173, 220	33, 84, 176, 227	27, 80, 172, 222	30, 86, 178, 224
18	112, 201	111, 198	112, 206	108, 197	38	115, 204	155	151	160	150	158
19	44, 110, 162, 222	43, 107, 159, 220	47, 113, 165, 225	40, 106, 158, 218	44, 115, 167, 227	39	155	151	158	150	159
20	56, 131, 208	56, 133, 205	55, 136, 212	50, 127, 203	57, 134, 210	40	154	150	159	150	150

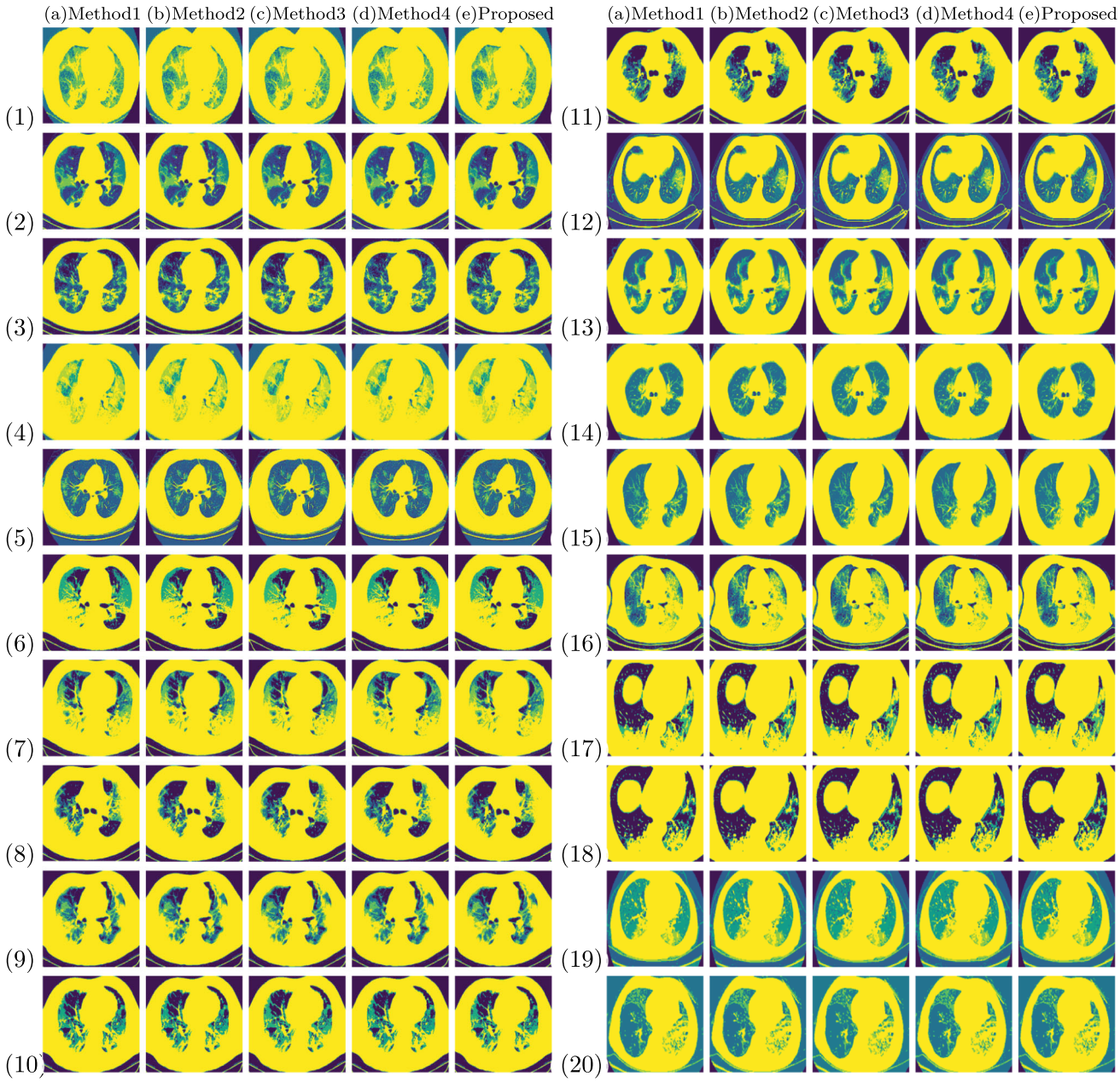

Fig. 6 Segmentation results: Lungs affected by above 50% due to COVID-19

3.2 Root-mean-square error (RMSE)

The metric RMSE has implemented to enumerate the root-mean-square error value of the image. If an image has an eminent quality, then the RMSE value should be near to zero. The RMSE signified by the mathematical design is as below

$$RMSE = \sqrt{\frac{1}{\mathbb{R} \times \mathbb{C}} \sum_{r=1}^{\mathbb{R}} \sum_{c=1}^{\mathbb{C}} \left(\mathbb{A}^{seg}(r,c) - \mathbb{B}^{seg}(r,c) \right)^2} \tag{17}$$

where the symbols $\mathbb{R}, \mathbb{C}$ defines the number of rows and columns of the images $\mathbb{A}^{seg}$ and $\mathbb{B}^{seg}$ respectively.

Table 2 MAE Values

Lungs affected by above 50% due to COVID-19						Lungs affected by below 50% due to COVID-19					
S.no	Method1	Method2	Method3	Method4	Proposed	S.no	Method1	Method2	Method3	Method4	Proposed
1	0.1747	0.0895	0.2377	0.2997	0.0433	21	0.1482	0.1223	0.1499	0.1334	0.0855
2	0.1638	0.1423	0.1708	0.0747	0.0389	22	0.1189	0.1015	0.1517	0.1355	0.0751
3	0.1583	0.2164	0.2583	0.1772	0.0610	23	0.1348	0.1101	0.1477	0.0981	0.0469
4	0.1287	0.2161	0.1414	0.1687	0.0337	24	0.1107	0.0888	0.1275	0.1050	0.0488
5	0.0703	0.1605	0.1403	0.1355	0.0355	25	0.0830	0.0653	0.1245	0.1163	0.0482
6	0.0642	0.1336	0.1462	0.1339	0.0336	26	0.1003	0.1249	0.1380	0.1145	0.0743
7	0.1257	0.1688	0.1756	0.0961	0.0456	27	0.1141	0.1299	0.1359	0.1199	0.1006
8	0.0979	0.1191	0.2408	0.2320	0.0414	28	0.1319	0.1022	0.1392	0.1297	0.0449
9	0.1398	0.1877	0.2548	0.0548	0.0402	29	0.1390	0.1104	0.1444	0.1150	0.1053
10	0.1371	0.0996	0.1499	0.2380	0.0795	30	0.1384	0.1311	0.1988	0.2101	0.1018
11	0.1132	0.1499	0.1428	0.1966	0.0803	31	0.0999	0.0724	0.1243	0.1338	0.0432
12	0.1178	0.1314	0.1422	0.1614	0.0918	32	0.1189	0.1106	0.1435	0.1065	0.0636
13	0.1386	0.1349	0.0886	0.1662	0.0501	33	0.1309	0.1019	0.1154	0.0998	0.0867
14	0.0559	0.1155	0.1398	0.1001	0.0162	34	0.1113	0.1045	0.1259	0.1013	0.0699
15	0.0715	0.1770	0.1344	0.1567	0.0470	35	0.1224	0.1016	0.1389	0.1189	0.0709
16	0.1821	0.1218	0.1943	0.1554	0.0620	36	0.1047	0.1194	0.1247	0.0846	0.0401
17	0.1178	0.0965	0.1285	0.1368	0.0388	37	0.0877	0.1237	0.1121	0.1337	0.0488
18	0.1368	0.1248	0.1001	0.1473	0.0399	38	0.1134	0.1060	0.1271	0.0734	0.0391
19	0.0812	0.1368	0.1212	0.1779	0.0411	39	0.1053	0.1330	0.1268	0.0873	0.0402
20	0.1005	0.1538	0.1358	0.1410	0.0833	40	0.1363	0.1020	0.1363	0.1363	0.0320

3.3 Correlation (CORR)

The other crucial factor is prescribed to assess the correlation of the two images like $\mathbb{A}^{seg}$ and $\mathbb{B}^{seg}$. The factor CORR is nominated by the following equ.

$$CORR = \frac{2\sum_{r=1}^{\mathbb{R}}\sum_{c=1}^{\mathbb{C}}\mathbb{A}^{seg}(r,c)\mathbb{B}^{seg}(r,c)}{\sum_{r=1}^{\mathbb{R}}\sum_{c=1}^{\mathbb{C}}(\mathbb{A}^{seg}(r,c))^2+\sum_{r=1}^{\mathbb{R}}\sum_{c=1}^{\mathbb{C}}(\mathbb{B}^{seg}(r,c))^2} \tag{18}$$

The largest value of *CORR* estimates the superior thresholding results. Aforementioned equation (18) delivers the outcome as 1 which mean that the images $\mathbb{A}^{seg}$ and $\mathbb{B}^{seg}$ are identical. Besides, if it returns the value of 0, then the images are not identical.

3.4 Signal to noise ratio (SNR)

$$SNR = 10\log_{10}\left[\frac{\sum_{r=1}^{\mathbb{R}}\sum_{c=1}^{\mathbb{C}}(\mathbb{B}^{seg}(r,c))^2}{\sum_{r=1}^{\mathbb{R}}\sum_{c=1}^{\mathbb{C}}(\mathbb{B}^{seg}(r,c)-\mathbb{A}^{seg}(r,c))^2}\right] \tag{19}$$

The huge value of *SNR* reveals the excellent outcome because both the images $\mathbb{A}^{seg}$ and $\mathbb{B}^{seg}$ are identical.

3.5 Peak signal to noise ratio (PSNR)

$$PSNR = 10\log_{10}\left[\frac{255^2}{\frac{1}{\mathbb{RC}}\sum_{r=1}^{\mathbb{R}}\sum_{c=1}^{\mathbb{C}}(\mathbb{B}^{seg}(r,c)-\mathbb{A}^{seg}(r,c))^2}\right] \tag{20}$$

The supreme value of *PSNR* exposes the superior effect because both the images $\mathbb{A}^{seg}$ and $\mathbb{B}^{seg}$ are equivalent.

4 Experimental results and analysis

The capability of the proposed PFS-based thresholding scheme has been inspected in several lungs affected due to COVID-19 (above 50% and below 50%) images. In order to exhibit the great performance of the proposed scheme, it is compared with four methods namely Method1 [4], Method2 [5], Method3 [6], and Method4 [7], several

Table 3 RMSE Values

Lungs affected by above 50% due to COVID-19						Lungs affected by below 50% due to COVID-19					
S.no	Method1	Method2	Method3	Method4	Proposed	S.no	Method1	Method2	Method3	Method4	Proposed
1	0.1768	0.1452	0.2378	0.2583	0.0455	21	0.1497	0.1169	0.1558	0.1495	0.0782
2	0.1168	0.0189	0.216	0.0941	0.0654	22	0.1359	0.0999	0.1498	0.147	0.0871
3	0.1850	0.2380	0.2533	0.1983	0.0305	23	0.1348	0.1161	0.1559	0.0959	0.0638
4	0.1336	0.2128	0.1440	0.1740	0.0036	24	0.1351	0.0991	0.1357	0.1106	0.0757
5	0.0984	0.1762	0.1463	0.1156	0.0442	25	0.1132	0.0734	0.1393	0.1230	0.0559
6	0.0778	0.1283	0.1535	0.1477	0.0365	26	0.1359	0.1143	0.1444	0.0847	0.0657
7	0.1417	0.1749	0.1958	0.0998	0.0331	27	0.1115	0.1224	0.1396	0.1196	0.0905
8	0.1231	0.1670	0.2231	0.1903	0.0618	28	0.1276	0.0976	0.1343	0.1013	0.0573
9	0.1575	0.1704	0.2202	0.0537	0.0306	29	0.1395	0.1145	0.1407	0.1200	0.1034
10	0.1201	0.0911	0.1302	0.2503	0.0572	30	0.2146	0.1973	0.2548	0.2634	0.0900
11	0.1134	0.1640	0.1389	0.1891	0.0911	31	0.1164	0.0968	0.1267	0.1416	0.0557
12	0.1033	0.1187	0.1363	0.1565	0.0923	32	0.1245	0.1193	0.1751	0.1008	0.0751
13	0.1395	0.1230	0.0959	0.1642	0.0452	33	0.1215	0.1071	0.1452	0.0998	0.0698
14	0.0656	0.1143	0.1315	0.0989	0.0116	34	0.1171	0.1129	0.1215	0.1062	0.0771
15	0.0977	0.1945	0.1431	0.1657	0.0588	35	0.1137	0.0977	0.1288	0.1088	0.0723
16	0.1785	0.1218	0.1854	0.1441	0.0697	36	0.1083	0.1252	0.1311	0.0859	0.0372
17	0.1159	0.0912	0.1294	0.1294	0.0353	37	0.0942	0.1178	0.1013	0.1305	0.0466
18	0.1279	0.1113	0.0978	0.1456	0.0383	38	0.1195	0.1095	0.1256	0.0872	0.0306
19	0.0714	0.1252	0.1116	0.1668	0.0366	39	0.1099	0.1235	0.1124	0.0955	0.0355
20	0.1102	0.1442	0.1267	0.1353	0.0922	40	0.1465	0.1087	0.1465	0.1465	0.0339

quality measurement factors examined in the before-mentioned section have been applied. The values of the quality measurement factors reveal that the outcomes of the proposed method produce a greater efficiency than recent sophisticated methods. Besides, the addressed method signifies the minimal error, high similarity, and is very convenient for real-time applications. Also, the proposed scheme would be highly beneficial in terms of image quality.

Initially, the dataset contains the CT scan of lungs affected by COVID-19 that can be found at the following link: https://github.com/UCSD-AI4H/COVID-CT. For this investigation, more than 50% and less than 50% of the lungs infected due to COVID-19 were taken for the experimental analysis. Then, Fig. 2 presents the source RGB images and it includes both the above and the below 50% infected lungs images due to COVID-19. The resolution of these images are 210×150, 275×193, 273×192, 343×188, 250×190, and so on. Further, the Red, Green, and Blue channels of source images were remodeled into grayscale images, and these converted images are exhibited in Fig. 3 (1a)–(4j). Meanwhile, Fig. 4 (1a)–(2j) exposes the histogram of the above 50% affected lungs due to COVID-19. In the same way, the histogram of remaining below 50% affected lungs due to COVID-19 are given in the same Fig. 4 (3a)–(4j). Later, PFS based enhancement scheme is implemented for Fig. 3 (1a)–(4j), then the enhanced images are displayed in Fig. 5 (1a)–(4j).

In addition, the values of the threshold for an enhanced first dataset (Fig. 5 (1a)) of above 50% affected lungs owing to COVID-19 images are determined by employing some other object extraction schemes and the proposed scheme, which are shown in the first row and second to sixth columns of Table 1. Then, Fig. 6 (1a)–(1e) provides object separated first dataset (Fig. 5 (1a)) of affected lungs images owing to COVID-19 after activating the current sophisticated methods, and proposed PFS method, respectively. From Fig. 6 (1e), it is clear that the proposed method is much improved and that it separates the foreground of the first dataset of affected lungs due to COVID-19. The values of the error in object extraction are estimated by analyzing the image mentioned above with the manually extracted object image. In this, two types of error rating factors such as MAE, and RMSE are applied, and these estimated error values are portrayed in the first row

Table 4 CORR Values

Lungs affected by above 50% due to COVID-19						Lungs affected by below 50% due to COVID-19					
S.no	Method1	Method2	Method3	Method4	Proposed	S.no	Method1	Method2	Method3	Method4	Proposed
1	0.8518	0.8777	0.8501	0.8666	0.9145	21	0.8503	0.8831	0.8412	0.8506	0.9218
2	0.8811	0.8985	0.8483	0.8645	0.9249	22	0.8641	0.9001	0.8502	0.8530	0.9129
3	0.8652	0.8899	0.8523	0.9019	0.9531	23	0.8652	0.8839	0.8441	0.9041	0.9362
4	0.8893	0.9112	0.8725	0.8950	0.9512	24	0.8649	0.9009	0.8643	0.8894	0.9243
5	0.9170	0.9347	0.8755	0.8837	0.9257	25	0.8868	0.9266	0.8637	0.8770	0.9441
6	0.8997	0.8751	0.8620	0.8855	0.9518	26	0.8641	0.8857	0.8556	0.9153	0.9343
7	0.8859	0.8701	0.8644	0.8801	0.9899	27	0.8885	0.8776	0.8604	0.8804	0.9095
8	0.8610	0.8978	0.8608	0.8703	0.9551	28	0.8724	0.9024	0.8657	0.8987	0.9427
9	0.9001	0.8896	0.8556	0.8850	0.8947	29	0.8605	0.8855	0.8593	0.8800	0.8966
10	0.8616	0.8689	0.8012	0.7899	0.8942	30	0.7854	0.8027	0.7452	0.7366	0.9100
11	0.9001	0.9276	0.8757	0.8662	0.9568	31	0.8836	0.9032	0.8733	0.8584	0.9443
12	0.8811	0.8894	0.8565	0.8935	0.9364	32	0.8755	0.8807	0.8249	0.8992	0.9249
13	0.8691	0.8984	0.8846	0.9018	0.9133	33	0.8785	0.8929	0.8548	0.9002	0.9302
14	0.8887	0.8955	0.8741	0.8987	0.9301	34	0.8829	0.8871	0.8785	0.8938	0.9229
15	0.8776	0.8984	0.8611	0.8811	0.9291	35	0.8863	0.9023	0.8712	0.8912	0.9277
16	0.8953	0.8806	0.8753	0.9154	0.9599	36	0.8917	0.8748	0.8689	0.9141	0.9628
17	0.9123	0.8763	0.8879	0.9337	0.9512	37	0.9058	0.8852	0.8987	0.8695	0.9534
18	0.8866	0.8940	0.8729	0.9266	0.9609	38	0.8805	0.8905	0.8744	0.9128	0.9694
19	0.8947	0.8670	0.8732	0.9127	0.9598	39	0.8901	0.8765	0.8876	0.9045	0.9645
20	0.8637	0.8980	0.8637	0.8637	0.9680	40	0.8535	0.8913	0.8535	0.8535	0.9661

and second to sixth columns in Tables 2 and 3, whereas the CORR, SNR, and PSNR values are enumerated, which are also presented in the first row and second to sixth columns in Tables 4, 5, and 6. At last, the obtained MAE, RMSE, SNR, PSNR, and CORR metrics with distinct methods are plotted in the form of graphs, which are displayed in Fig. 8 (a)–(e).

On the other hand, the threshold values for an enhanced twenty-first dataset (Fig. 5 (3a)) of the below 50% affected lungs due to COVID-19 images are acquired by several methods, which are provided in the first row and seventh to twelfth columns of Table 1. After implementing such mentioned methods, the foreground of the enhanced lungs affected due to COVID-19 (below 50%) image is extracted and the resulting foregrounds are presented in Fig. 7 (1a)–(1e). Utilizing the resultant foregrounds, the quality measurement factors like MAE, RMSE, SNR, PSNR, and CORR are quantified and these measured values are arranged in a first row and seventh to twelfth columns in Tables 2, 3, 4, 5 and 6. Subsequently, the measured/tabulated outcomes are depicted as the plotted graphs, and these graphs are shown in Fig. 8 (a)–(e). From the mentioned row and columns of Tables 23, 4, 5, 6 and Fig. 8 (a)−(e), the proposed scheme establishes the great outcomes by generating smaller MAE and RMSE error values as well as larger SNR, PSNR, and CORR values.

In the same manner, employing the maximum similarity principle [32], the enhanced images of all remaining affected lungs (above 50%) due to COVID-19 (Fig. 5 (1b)–(2j)) are thresholded, and these depicted thresholds are listed in rows second to twenty and columns second to sixth in Table 1. By presenting the methods of Method1 [4], Method2 [5], Method3 [6], and Method4 [7], the foregrounds of the enhanced images (Fig. 5 (1b)–(2j)) are separated and these foregrounds are pictured in Fig. 6 [(2a) – (2d)] –[(20a) –(20d)]. In the final analysis, Fig. 6 (2e)–(20e) illustrates the output images found after the foreground extraction procedure by implementing the proposed scheme. Four unique methods and the experimental outcomes of the proposed method are analyzed, and this reveals that the proposed PFS method devotes the preferable thresholded image rather than current state-of-the-art methods. Further, the aforementioned metric values of current sophisticated object extraction methods along with the proposed PFS scheme are assessed, and these values are listed in rows second to twenty and columns second to

Table 5 SNR Values

Lungs affected by above 50% due to COVID-19						Lungs affected by below 50% due to COVID-19					
S.no	Method1	Method2	Method3	Method4	Proposed	S.no	Method1	Method2	Method3	Method4	Proposed
1	30.2795	31.4671	29.7634	29.3539	38.1155	21	33.9469	43.1464	30.2547	39.8896	43.3880
2	27.1287	30.0022	24.7597	30.8938	31.4140	22	29.6637	30.0032	26.0317	29.5251	33.2055
3	29.7050	28.0634	26.6666	29.3787	32.9996	23	27.3431	31.3192	26.0751	32.0396	32.8634
4	34.8717	30.8854	33.9301	33.0058	40.0879	24	27.1899	29.3318	25.6493	28.4965	34.8070
5	31.6884	26.2796	26.4073	26.5656	33.7392	25	31.2269	31.3540	26.1195	30.6787	31.5431
6	34.2012	34.1761	29.7095	33.6803	34.692	26	30.0556	30.2343	28.3104	33.7267	33.8192
7	31.8016	30.6639	30.4125	31.8792	34.0530	27	28.7550	26.6027	24.6660	28.2279	29.7156
8	35.5087	33.3149	30.6727	31.5015	36.9881	28	27.9877	33.4709	24.9627	28.4256	34.0161
9	33.4174	32.2572	29.5881	34.0522	40.2179	29	27.5117	30.4978	24.7644	28.6493	30.5374
10	41.3918	45.1275	30.1715	30.1501	46.4429	30	25.3280	25.9258	23.3840	13.3833	29.5742
11	35.8235	31.0173	30.7402	31.0426	37.2599	31	30.87310	31.8320	30.1029	29.1264	40.0524
12	26.5883	24.5840	26.5509	26.0203	39.5524	32	30.0267	31.9283	28.5942	34.0071	34.3914
13	29.9359	30.6498	30.9091	28.9729	34.0707	33	22.5232	30.0969	23.8126	34.2866	35.2147
14	31.8935	30.1665	28.8289	30.1357	40.8906	34	29.2781	30.6594	28.8645	33.7673	35.2704
15	33.4366	28.6358	30.9143	28.8457	37.6894	35	30.5853	34.3945	29.2075	31.4291	36.4308
16	29.6091	33.5796	27.2368	31.5312	34.7766	36	30.5887	30.2365	29.2697	36.0926	38.9746
17	34.0592	34.4255	31.4066	31.4066	41.7385	37	33.6434	31.9200	32.5331	29.3574	41.5685
18	34.5088	34.5102	34.7131	29.9947	34.8169	38	36.4994	38.4475	34.9413	44.0832	50.6463
19	33.6613	28.1026	29.4326	26.3910	33.9885	39	34.6914	29.4974	33.3607	40.6365	44.0857
20	31.4479	26.2605	28.4942	27.6002	37.3982	40	34.0977	40.1592	34.0977	34.0977	43.2307

Table 6 PSNR Values

Lungs affected by above 50% due to COVID-19						Lungs affected by below 50% due to COVID-19					
S.no	Method1	Method2	Method3	Method4	Proposed	S.no	Method1	Method2	Method3	Method4	Proposed
1	31.1725	32.3601	30.6565	30.2470	39.0086	21	35.5923	45.0334	31.9000	41.5349	44.7914
2	28.5857	31.4593	26.2167	32.3508	32.871	22	31.5339	31.8734	27.9019	31.3953	35.0757
3	31.4065	29.7649	28.3681	31.0803	34.7011	23	29.1371	33.1132	27.8691	33.8336	34.6574
4	35.3729	31.3867	34.4313	33.5070	40.5892	24	28.9508	31.0926	27.4104	30.2574	36.5679
5	33.9344	28.5256	28.6532	28.8115	35.9852	25	32.9536	33.2698	27.8462	32.4054	33.0807
6	35.3134	35.2883	30.8217	34.7925	35.8042	26	32.6927	32.8713	30.9474	36.3638	36.4562
7	32.8699	31.7322	31.4808	32.9475	35.1213	27	30.6999	28.5476	26.6108	30.1727	31.6605
8	36.7597	34.5658	31.9237	32.7525	38.2391	28	30.5130	35.9961	27.4880	30.9509	36.5414
9	34.6512	33.4910	30.8220	35.2860	41.4518	29	29.8545	32.8406	27.1072	30.9921	32.8802
10	42.5964	46.3321	31.3761	31.3547	47.6475	30	29.1101	29.7079	27.1662	17.1655	33.3564
11	37.3259	32.5196	32.2426	32.5449	38.7622	31	33.4164	34.3754	32.6463	31.6698	42.5957
12	29.5811	27.5768	29.5437	29.0131	42.5452	32	32.9467	34.8483	31.5142	36.9271	37.3114
13	31.3586	32.0726	32.3319	30.3957	35.4935	33	25.669	33.2427	26.9583	37.4323	38.3604
14	33.0627	31.3358	29.9981	31.3050	42.0599	34	31.8287	33.2100	31.4151	36.3180	37.8211
15	34.6070	29.8062	32.0847	30.0160	38.8599	35	32.7747	36.4839	31.2968	33.5185	38.5201
16	31.2098	35.1802	28.8375	33.1318	36.3772	36	33.0349	32.6827	31.7158	38.5388	41.4208
17	34.7893	35.1556	32.1367	32.1367	42.4686	37	36.9057	35.1823	35.7954	32.6197	44.8308
18	35.4858	35.4871	35.6901	30.9717	35.7939	38	37.8515	39.7996	36.2935	45.4353	46.9984
19	35.3693	29.8106	31.1406	28.099	35.6965	39	36.1114	40.9175	34.7807	42.0565	45.5057
20	33.0771	27.8897	30.1234	29.2293	39.0274	40	35.6784	41.7398	35.6784	35.6784	44.8114

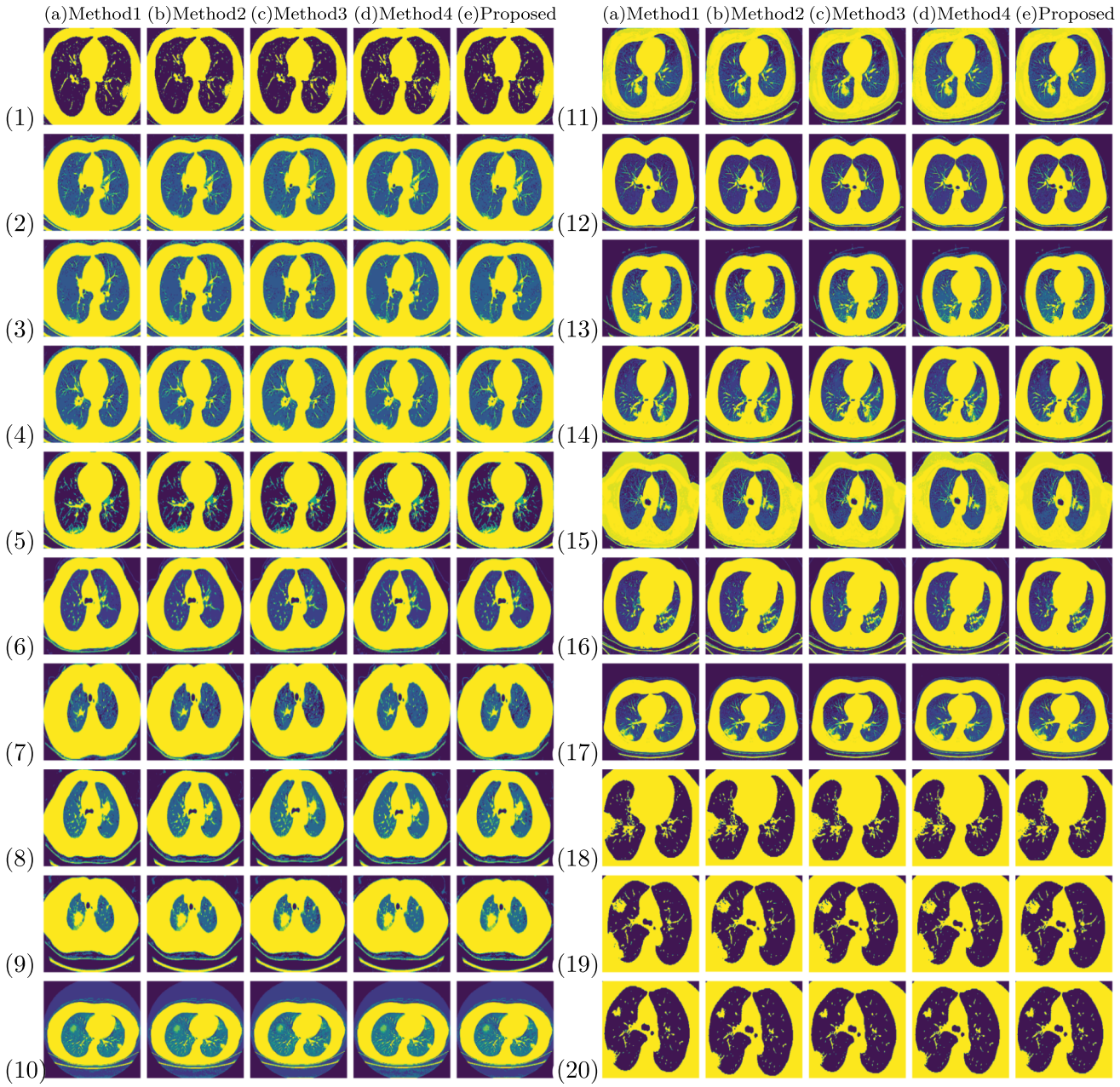

Fig. 7 Segmentation results: Lungs affected by below 50% due to COVID-19

sixth in Tables 2, 3, 4, 5 and 6. Moreover, the listed values are drawn as the plotted graph, which is exhibited in Fig. 8 (a)–(e). From Tables 2, 3, 4, 5, 6 and Fig. 8 reports that the foreground separation received by the proposed PFS scheme exceeds other methods mentioned.

Likewise, the remaining images of below 50% affected lungs due to COVID-19 are enhanced then the resultant images are given in Fig. 5 (3b)–(4j). Further to that, the obtained images were utilized for the purpose of the extraction process, which determines the thresholds that are exhibited in rows second to twenty and columns seventh to twelfth in Table 1. Besides, using recent sophisticated techniques as well as the proposed one to segment the images, which are depicted in Fig. 7 [(2a) –(2e)]– [(20a) –(20e)]. After the segmentation, we employed some evaluation metrics to compute MAE, RMSE, CORR, SNR, and PSNR values then they are tabulated in rows second to twenty and seventh to twelfth columns in Tables 2, 3, 4, 5 and 6. Following the Tables, the values are as plotted as graphical forms, which are shown in Fig. 8 (a)–(e). Figs. 7, 8, and Tables 2, 3, 4, 5 and 6 are evidenced to display the performance of the addressed method.

In general, Tables 2 and 3, and Fig. 8 (a)–(b) exhibit the quality measurement factor values found after

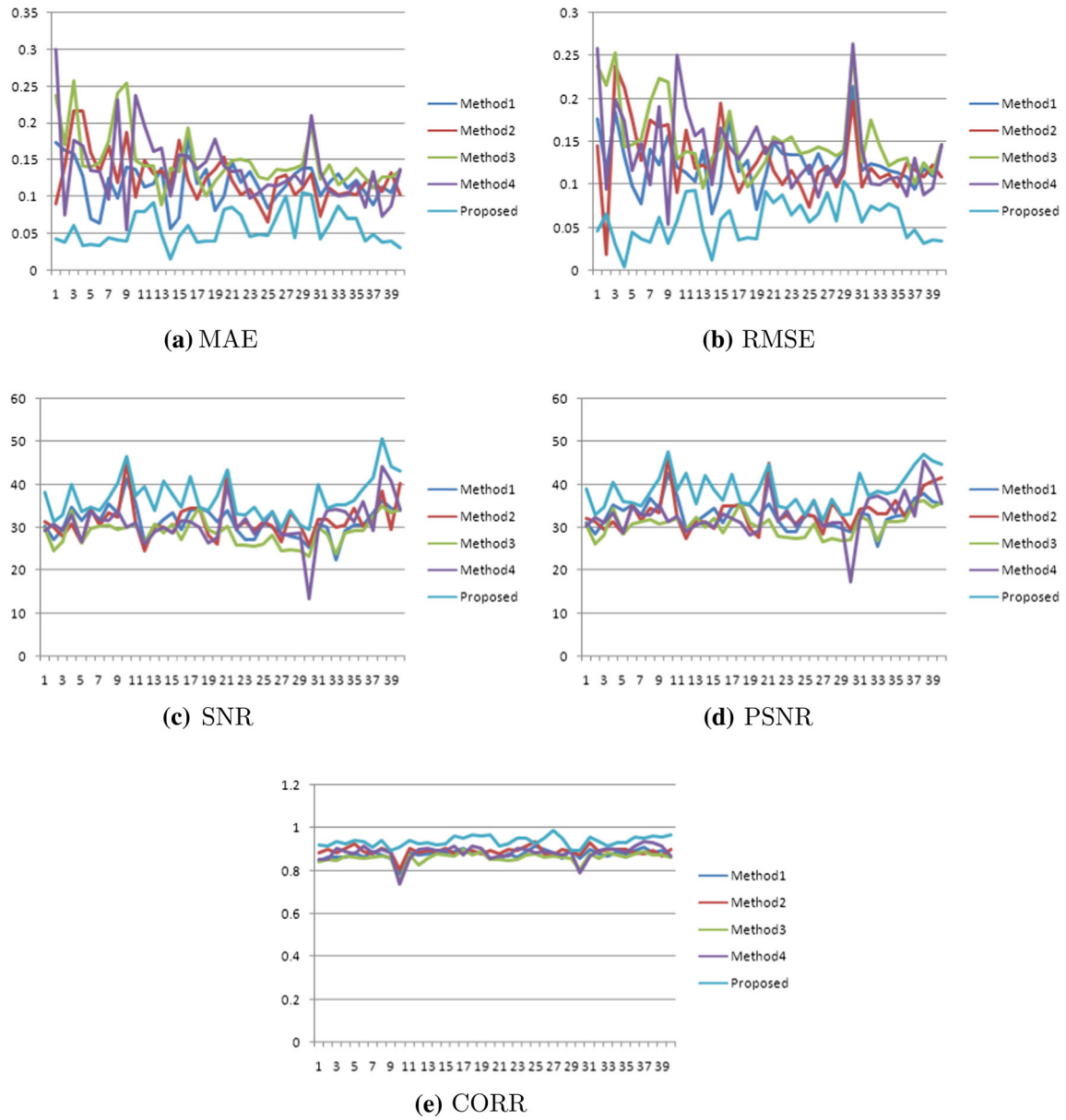

Fig. 8 Evaluation Metrices

implementing various segmentation schemes in enhanced images of lungs affected due to COVID-19. It is noteworthy that from the values in the aforementioned tables, the proposed PFS scheme delivers minimal error values compared to the state-of-the-art methods. The maximum CORR values (Table 4) for the proposed scheme confirm that the object in the enhanced images (above and below 50%) of lungs affected due to COVID-19 is clearly separated. Although the first and second sophisticated methods hold the big CORR values, the visual quality of the resulting images gained by the proposed scheme outperforms other methods. Furthermore, it is obvious from the values in Tables 4, 5 and 6 that the proposed method yields higher SNR, CORR, and PSNR values compared to the mentioned current sophisticated methods. The difference between the proposed and state-of-the-art techniques

shows the maximum values, which are the reasons mentioned to determine that the proposed PFS thresholding scheme is most worthy for all images of lungs infected owing to COVID-19.

5 Conclusion

Recent developments in image analysis for digital images such as image enhancement and division have been surveyed in the construction of PFS and FS theory. This research paper deals with the perusal and structure of the segmentation scheme related to the PFS feature of lung infected owing to COVID-19 images. The recommended object segmentation scheme develop image enhancement and thresholding technique. By employing the PFS entropy, the considered images are enhanced, and it exhibits adequate quality images. Besides, the successful implementation of quality measurement factors will lead to some significant improvements in image quality as the PFS-based segmentation scheme is attractive, which makes the proposed scheme more relevant and ensures image quality if the image is considered blurry / noise. Therefore, such work would be important for efforts to discover a more beneficial scheme for image segment analysis.

Acknowledgements This paper is partly supported by the Department of Science and Technology (DST)-Promotion of University Research and Scientific Excellence (PURSE) Phase-II, Government of India, New Delhi (Memo No. BU/DST PURSE (II)/APPOINTMENT/515).

Declaration

Conflict of interest The authors declare that they have no known competing financial interests or personal relationships that could have appeared to influence the work reported in this paper.

References

1. Ahmadi M, Sharifi A, Dorosti S, Jafarzadeh Ghoushchi S, Ghanbari N (2020) Investigation of effective climatology parameters on COVID-19 outbreak in Iran. Sci Total Environ. 729:138705
2. Wang X, Deng X, Fu et al (2020) A weakly-supervised framework for COVID-19 classification and lesion localization from chest CT. IEEE Trans Med Imag. 39(8):2615–2625
3. Wang G, Liu X, Li et al (2020) A noise-robust framework for automatic segmentation of COVID-19 pneumonia lesions from CT images. IEEE Trans Med Imag. 39(8):2653–2663
4. Li L, Sun L, Xue Y, Li S, Mansour RF (2021) Fuzzy multilevel image thresholding based on improved coyote optimization algorithm. IEEE Access 9:33595–33607
5. Houssein EH, Emam MM, Ali AA (2021) Improved manta ray foraging optimization for multi-level thresholding using COVID-19 CT images. Neural Comput Appl. 33:16899–16919
6. Hassanien AE, Mahdy LN, Ezzat KA, Elmousalami HH, Ella HA (2020) Automatic x-ray covid-19 lung image classification system based on multi-level thresholding and support vector machine,medRxiv
7. Abualigah L, Diabat A, Sumari P, Gandomi AH (2021) A Novel Evolutionary Arithmetic Optimization Algorithm for Multilevel Thresholding Segmentation of COVID-19 CT Images, processes, Vol. 9, PP. 1155
8. Elaziz MA, Ewees AA, Yousri et al (2020) An improved marine predators algorithm with fuzzy entropy for multilevel thresholding: real world example of covid-19 CT image segmentation. IEEE Access. 8:125306–125330
9. Dibya JB, Thakur RS (2018) An Efficient Technique for Medical Image Enhancement Based on Interval Type-2 Fuzzy Set Logic. Progress Comput, Analyt Network. 710:667–678
10. Borra S, Thanki R, Dey N (2019) Satellite image enhancement and analysis. In: Satellite image analysis: clustering and classification. SpringerBriefs in Applied Sciences and Technology, Springer, Singapore. https://doi.org/10.1007/978-981-13-6424-2_2
11. Ram BSB, Senthilkumaran P, Sharma A (2017) Polarization based spatial filtering for directional and nondirectional edge enhancement using S-waveplate. Appl opt. 56:3171–3178
12. Ullah Z, Farooq MU, Lee S-H, An D (2020) A hybrid image enhancement based brain MRI images classification technique. Med Hypoth. 143:109922
13. Zhong S, Jiang X, Wei J, Wei Z (2013) Image enhancement based on wavelet transformation and pseudo-color coding with phase-modulated image density processing. Infrared Phys Technol. 58:56–63
14. Chaira T (2014) Enhancement of medical images in an Atanassovs intuitionistic fuzzy domain using an alternative intuitionistic fuzzy generator with application to image segmentation. J Intell Fuzzy Syst. 27(3):1347–1359
15. Bhandari AK, Kumar A, Singh GK (2015) Improved knee transfer function and gamma correction based method for contrast and brightness enhancement of satellite image. AEU-Int J Electr Commun. 69(2):579–589
16. Yacin Sikkandar M, Alrasheadi BA, Prakash NB et al (2021) Deep learning based an automated skin lesion segmentation and intelligent classification model. J Ambient Intell Human Comput. 12:3245–3255
17. Nie F, Zhang P, Li J, Ding D (2017) A novel generalized entropy and its application in image thresholding. Signal Process. 134:23–34
18. Kaur T, Saini BS, Gupta S (2016) Optimized multi threshold brain tumor image segmentation using two dimensional minimum cross entropy based on co-occurrence matrix, Medical imaging in clinical applications, PP. 461-486
19. Zadeh LA (1965) Fuzzy sets. Inf Control. 8:338–356
20. Bustince H, Barrenechea E, Pagola M (2007) Image thresholding using restricted equivalence functions and maximizing the measures of similarity. Fuzzy Sets Syst. 158(5):496–516
21. Chaira T (2010) Intuitionistic fuzzy segmentation of medical images. IEEE Trans Biomed Eng. 57(6):1430–1436
22. Ananthi VP, Balasubramaniam P (2016) A new thresholding technique based on fuzzy set as an application to leukocyte nucleus segmentation, Computer Methods and Programs in Biomedicine.https://doi.org/10.1016/j.cmpb.2016.07.002.
23. Atanassov KT (1986) Intuitionistic fuzzy sets. Fuzzy Sets Syst. 20:87–96
24. Yager RR (2013) Pythagorean fuzzy subsets. Proceeding of The Joint IFSA World Congress and NAFIPS Annual Meeting. Edmonton, Canada, pp 57–61
25. Yager RR (2014) Pythagorean membership grades in multicriteria decision making. IEEE Trans Fuzzy Syst. 22:958–965

26. Raj S, Vinod DS, Mahanand BS et al (2020) Intuitionistic fuzzy C means clustering for lung segmentation in diffuse lung diseases. Sens Imag. 21(37):1–16
27. Yager RR (1979) On the measure of fuzziness and negation, part I: membership in the unit interval. Int J Gen Syst. 5:221–229
28. Yager RR (1980) On a general class of fuzzy connectives. Fuzzy Sets Syst. 4(3):235–242
29. Yanhui G, Abdulkadir SE (2014) A novel image segmentation algorithm based on neutrosophic similarity clustering. Appl Soft Comput. 25:391–398
30. Arindam J, Garima S, Rashmi M, Madhumala G, Amit K, Chandan C, Atulya KN (2014) Automatic leukocyte nucleus segmentation by intuitionistic fuzzy divergence based thresholding. Micron. 58:55–65
31. Yanhui G, Abdulkadir S, Ye J (2014) A novel image thresholding algorithm based on neutrosophic similarity score. Measurement. 58:175–186
32. Li Z, Lu M (2019) Some novel similarity and distance measures of pythagorean fuzzy sets and their applications. J Intell Fuzzy Syst. 37(2):1781–1799
33. Qiang Z, Junhua H, Jinfu F, Liu A, Yongli L (2019) New similarity measures of pythagorean fuzzy sets and their applications. IEEE Access. https://doi.org/10.1109/ACCESS.2019.2942766
34. Peng X (2019) New similarity measure and distance measure for Pythagorean fuzzy set. Complex and Intell Syst. 5(5):101–111
35. Peng XD, Yuan H, Yang Y (2017) Pythagorean fuzzy information measures and their applications. Int J Intell Syst. 32(10):991–1029
36. Luca DA, Termini (1972) Definition of non probabilistic entropy in the setting of fuzzy set theory. Inform Control. 20(461):301–312